ISSN 2063-5346

UNRAVELLING THE GREEN ELECTRICITY GENERATION USING NANOCRYSTALLINE ZN-MG FERRITE BASED HYDROELECTRIC CELL: AN EMERGING ENERGY HARVESTER

Vivek Kumar [1], Rakesh Kumar Singh [1*], Pammi Kumari [1], Rajan Kumar [1], Aniket Manash [1, 2], Jyoti Shah [3], R K Kotnala [3]

Article History: Received: 01.02.2023 Revised: 07.03.2023 Accepted: 10.04.2023

Abstract:

A new idea in energy harvesting is to employ hydroelectric cells (HECs) to produce cleaner energy from water dissociation. Hydroelectric cells are beneficial and eco-friendly inventions of this century, which dissociate water molecules to generate electricity without an electrolyte. In this study, a sol-gel method was used to synthesize $Mg_{0.7}Zn_{0.3}Fe_2O_4$ nanoferrite in order to construct a hydroelectric cell that produces electricity by the dissociation of water molecules. X-ray diffraction revealed the cubic crystal structure (Fd-3m space group) with a crystallite size of 30.79 nm, approximately. For water to split on the surface of ferrite, substantial water absorption at 1638 and 3438 cm^{-1}, and metal oxide bonds near 418 cm^{-1} and 547 cm^{-1} are shown by FTIR spectroscopy. FESEM imaging of the prepared ferrite with an average grain size of 91 nm exhibited porosity in the prepared ferrite, which is 40.2 % theoretically by XRD studies. The crystallographic defects and O_2 (oxygen) vacancies required for water dissociation are shown in PL studies performed at room temperature. The impedance analysis demonstrated a semi-circular Nyquist plot and a small tail, which signifies the presence of a low charge transfer resistance and Warburg impedance, respectively. The described ferrite surface dissociates water into H_3O^+ and OH^- ions by an electrolytic chain reaction, creating a voltage across electrodes. The V-I polarization plot indicated the offload current, open circuit voltage and offload power of 7 mA, 0.823 V and 5.61 mW, respectively. The enhanced porosity, crystal defects and oxygen voids are responsible for the dissociation of water molecules for the generation of electricity in $Mg_{0.7}\ Zn_{0.3}\ Fe_2O_4$ fabricated hydroelectric cell.

Keywords: Hydroelectric cell; Magnesium Ferrite; Porosity; Oxygen vacancies; Impedance spectroscopy.

[1] Aryabhatta Center for Nanoscience and Nanotechnology, Aryabhatta Knowledge University, Patna 800001, Bihar, India.

[2] Department of Mechanical Engineering, Vidya Vihar Institute of Technology, Maranga, Purnea, Bihar-854303, India

[3] CSIR-National Physical Laboratory, Dr. K. S. Krishnan Road, New Delhi, 110012, India

[*] Corresponding Author: Rakesh Kumar Singh, (rakeshsinghpu@gmail.com)

DOI:10.31838/ecb/2023.12.s1-B.252

Introduction

The hydroelectric cells (HECs) have become an alternative eco-friendly energy source, which provide green electricity by the splitting the water molecules due to the oxygen deficiency in the nanoporous oxide materials [1]. The chemidissociation of H_2O on the surface results in the dissociation of water molecules in H_3O^+ and OH^- [2]. The hydroxide ions get chemically bonded with the unsaturated surface cations, and further dissociate the physisorbed water molecule, which are physically bonded by hydrogen bonds. The nanopores present in the oxide materials are responsible for the trapping of some OH^- ions, which generates sufficient electric potential [1-2]. The potential further dissociates the physically adsorbed water molecules into their respective ions, and movement of ions towards the electrodes generates electricity. The chemidissociation of water molecules is largely affected by O_2 vacancies and the surface cations present on the metal oxide surface [1-4]. Besides metal oxides, spinel ferrites have also been used to produce green electricity from HECs recently. Magnesium ferrite, which has the chemical composition $MgFe_2O_4$, has an extensive application in the fields of data storage, MRI, drug delivery, catalysis etc. due to some interesting characteristics like good chemical stability, moderate magnetization, and high electrical resistance [5-9]. There is a regular distribution of Mg^{2+} and Fe^{3+} s between tetrahedral (A-site) and octahedral (B-site) [10]. Kotnala et al. have investigated the defects and the porous microstructures present in the magnesium ferrites, which make it applicable as humidity sensors [11]. The surface of ferrite is rich in unsaturated surface cations and oxygen voids, which adsorb the other molecules such as water. Physiorption and chemisorption are the two adsorption processes. The substitution of the metal ions at the A or B site of the Magnesium ferrite creates the lattice distortion, which may affect the porosity and oxygen vacancies in the ferrites. This makes the metal substituted magnesium ferrite a potential candidate for hydroelectric cells. The extensive studies on ferrite fabricated HECs indicate an appreciable amount of generated electric currents. A research study explains that Li-substituted $MgFe_2O_4$ pellet (surface area 17 cm^2) provided current and power having values of 82 mA and 74 mW, respectively [12]. The $BaTiO_3$-$CoFe_2O_4$ nanoceramics fabricated HEC has generated the output current of 7.93 mA, described by Shah et al.[13]. An improvement in current densities (mA/cm^2) was perceived in Ni-Li ferrite HEC with current densities of 3.6 and 3.8 mA/cm^2 [14]. $NiFe_2O_4$ hydroelectric cells were analyzed by Kotnala et al. to yield 15.3 mA current [15]. Saini et al. have obtained the short circuit current ranging from 24 mA to 67 mA for the hydroelectric cells fabricated using lithium substituted nickel ferrite materials [16]. Manash et al. fabricated K^+ substituted Mg-ferrite and found the output current ranging from 1.4 to 7.8 mA [17]. Na-substituted $MgFe_2O_4$ based HECs were investigated by Kumar et al., where the offload currents were reported in the range 1.3-15 mA [18] Most of the studies have prepared the base material (ferrite or oxide) using solid state processing method. In this research sol-gel approach has been followed to prepared Zn-Mg nanoferrite. The HEC fabricated using zinc substituted magnesium ferrite has been investigated to observe the current and the power generation. The HEC fabrication using zinc substituted Mg-ferrite has not been done so far. A detailed impedance study of the prepared ferrite has been done to investigate the reasons of the current generation. Furthermore, the structural and optical characterizations have also been done for the defect related studies that may support the current generation in the fabricated HEC.

2. Materials and Method

2.1. Preparation of $Mg_{0.7}Zn_{0.3}Fe_2O_4$ materials

A sol gel auto-combustion technique has been adopted to prepare $Mg_{0.7}Zn_{0.3}Fe_2O_4$ materials, where magnesium nitrate [$Mg(NO_3)_2.6H_2O$), Fisher-Scientific, 99 %], Iron (III) Nitrate nonahydrate [$Fe(NO_3)_3.9H_2O$, Merk, 99 %], and citric acid monohydrate (Merck, 99%) were taken as starting compounds. The solution of these materials was prepared, and later appropriate mole of $Zn(NO_3)_2$ was added to the solution for the substitution of Zn^{2+} ions in the lattice. The solution was continuously stirred at 100 °C after adjusting the pH to 7 till the formation of a gel. Later, the gel was burnt in hot air oven, and further annealed at 800 °C to get reddish-brown ferrite powder. Figure 1 displays the synthesis process.

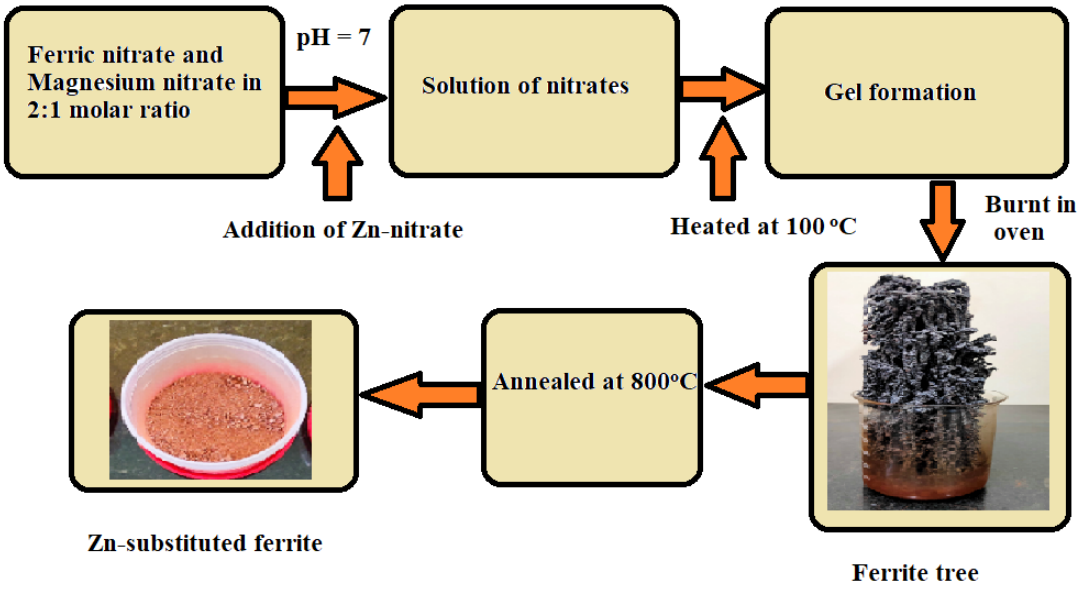

Fig. 1 Schematic of synthesis process

2.2. HEC (Hydroelectric cell) fabrication

In order to prepare the hydroelectric cell of the prepared ferrite materials, the pre-sintering of the obtained amorphous ferrite was done at 500 °C for 2 h and later crushed for 20 mins. Using a suitable binder (polyvinyl alcohol), the pellet of dimension 2.5 cm × 2.5 cm × 0.1 cm were formed and they were heat-treated at 800 °C for 1 h. For the formation of electrodes, one side of the pellet was zinc plated (anode), and opposite side was silver plated (cathode) in a unique comb like pattern. A schematic of fabricated hydroelectric cell is displayed in Fig. 2.

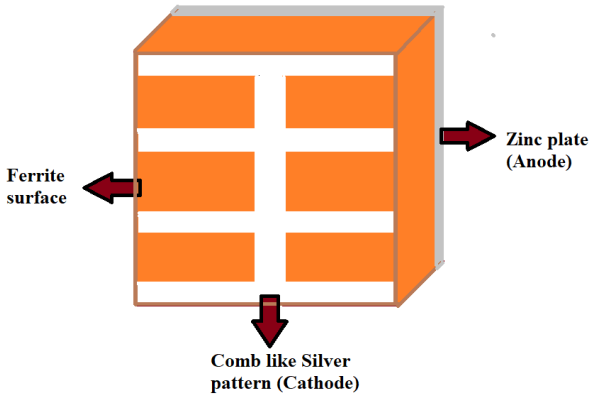

Fig. 2 A schematic of fabricated hydroelectric cell

2.3. Characterization

The phase analysis was done by XRD (Bruker, D8 Advance, Germany). The vibration bonds were observed using FTIR

spectroscopy (Perkin Elmer, UK). FESEM was used to observe the surface texture of the produced materials. The JEOL JEM 2100 was used to carry out HRTEM imaging. The emission wavelengths were examined using PL spectroscopy (Perkin Elmer, UK) at an appropriate excitation. The developed hydroelectric cell's V-I measurement was explored using a Keithley-2400 Source metre, and the produced ferrites' impedance was measured using a Wayne-Kerr Impedance Analyzer 6500B.

3. Results and discussion

3.1 X-Ray Diffraction

The XRD patters were observed by XRD with 4º /min scan rate in the 2θ angle ranging from 20 º to 70º. Fig. 3 shows the well crystalline $Mg_{0.7}Zn_{0.3}Fe_2O_4$ materials synthesized at 800 ºC for 2 h. The diffractograms of the $Mg_{0.7}Zn_{0.3}Fe_2O_4$ materials synthesized by sol-gel process reveal reflections (220), (311), (400), (422), (511) and (440) of Fd-3m space group (FCC cubic spinel), which confirms the magnesium ferrite phase (COD ID 9003776) without any impurity. The prominent maximum peak intensity plane was observed as (311) plane. The inter-planer d-spacing, lattice constant (a = b = c), cell volume (V), X-ray density (D_x), bulk density (D_b) and porosity (P) were calculated using the following relations [19, 20]:

$$n\lambda = 2dsin\theta, (1)$$

$$a = d[(h^2 + k^2 + l^2)]^{1/2}, (2)$$

$$V = a^3, (3)$$

$$D_x = \frac{8M}{Na^3}, (4)$$

$$D_b = \frac{M}{\pi r^2 h}, (5)$$

$$P\ \% = \left(1 - \frac{D_b}{D_x}\right) \times 100, (6)$$

where notations have their general meanings [19]

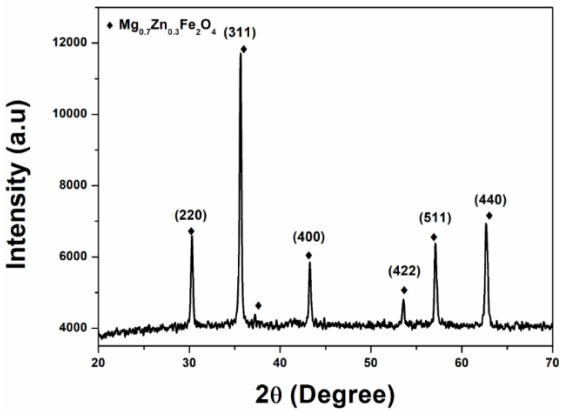

Fig. 3 XRD plot of Zn-Mg ferrite

The values of inter-planer d- spacing, lattice constant, cell volume, X-ray density, bulk density (D_b) and porosity (P) were found to be 2.5170 Å, 8.3479Å, 581.75 Å^3, 4.8467 g/cm^3, 2.182 and 40.2 %, respectively, which are in accordance with the ideal values of the cubic phase with a very small deviation, and represented in Table 1.

The average crystallite size with respect to the maximum peak intensity of the prepared ferrite was calculated from the Scherrer's formula (Equation 7) and found to be 30.79 nm.

$$t = \frac{0.9\lambda}{\beta \cos\theta}, (7)$$

where t is the crystallite size and other notations have their usual meanings.

Table 1. XRD parameters of $Mg_{0.7}Zn_{0.3}Fe_2O_4$ prepared at 800 ºC for 2 h

2θ	D (Å)	a=b=c (Å)	V (Å^3)	D_x (g/cm^3)	D_b (g/cm^3)	Porosity (%)	Crystallite size (nm)
35.64	2.5170	8.3479	581.75	4.8467	2.182	40.2	30.79

In order to study the lattice strains due to the zinc substitution, the Williamson-Hall plot was drawn, which is demonstrated in Fig. 4.

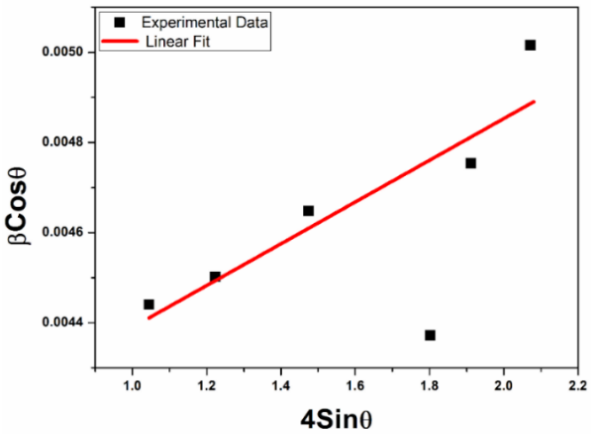

Fig. 4 W-H plot of magnesium ferrite with zinc substituted.

The W-H equation is represented as follows [19, 20]:

$$\beta \cos\theta = \frac{K\lambda}{D} + 4\varepsilon \sin\theta \text{ , (8)}$$

ε, D and β represent strain, average crystallite size and FWHM, respectively. The average crystallite size (D) has been found to be 35.28 nm from the value of the intercept ($\frac{K\lambda}{D}$) and the slope represents the lattice strain (ε), which is 4.63 × 10^{-4}. The micro strain creates lattice disorders leading to various crystallographic defects such as oxygen vacancies, unsaturated surface Fe^{3+} cations, grain boundary defects etc., which are responsible for water dissociation at room temperature. These are explained in the following sections of manuscript.

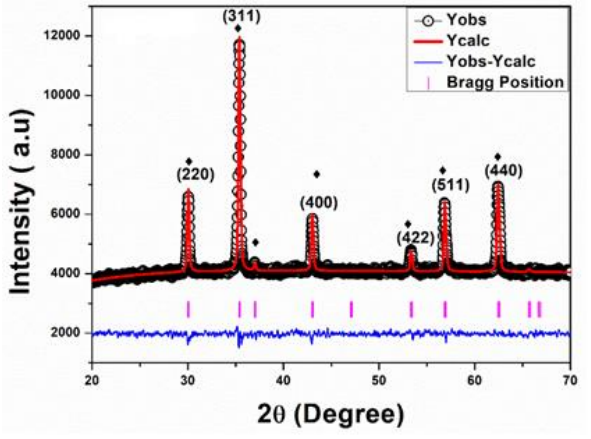

Fig. 5 Rietveld Refinement of $Mg_{0.7}Zn_{0.3}Fe_2O_4$ ferrite

Figure 5 shows the refined XRD patterns using Rietveld method, which indicates good fitting of XRD peaks with goodness of fit of 1.03. The refinement also indicates exact phase matching of the prepared Zn-Mg ferrite corresponding to the spinel magnesium ferrite with Fd-3m space group. The structural constraints obtained in the present research is significantly different from previously reported works on zinc substituted magnesium ferrites. George et al. have reported a lattice constant a = 8.41025 Å, crystallite size 40.41 nm and porosity 41.5 % of zinc substituted magnesium ferrite [21]. Compared to George et al., relatively lower lattice constant, lower crystallite size and a higher porosity has been obtained in our study. Powar et al. have found porosity ranging from 12 to 16 % of zinc substituted magnesium ferrite materials, which is very low as compared to the present study [22]. Abhishek et al. have found the lattice constant ranging from 8.41 to 8.44 Å of $Mg_{1-x}Zn_xFe_2O_4$ nanomaterials, which is higher than the lattice constant obtained in the present study [23]. Choodamani et al. have investigated the porosity between 15.6 and 16.51 % of Zn-Mg Ferrite, and crystallite size ranging from 47 to 80 nm [24]. But the present study shows a high porosity 40.2 %, and small crystallite size 30.79 nm.

3.2 Microstructure Analysis by FESEM:

Figure 6 represents the surface microstructure of the prepared ferrite. The microstructure seems agglomerated having good porosity. The increased agglomeration may be due to enhanced surface to volume ratio [25, 26].

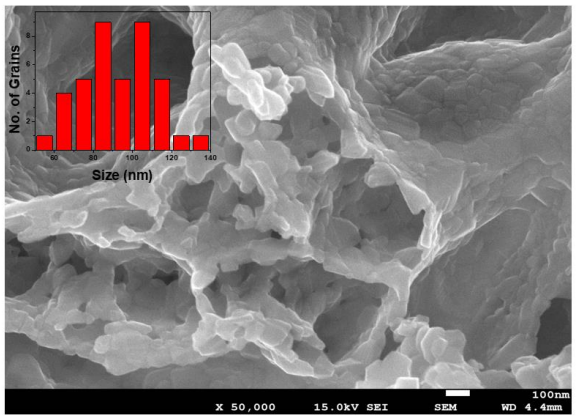

Fig. 6 FESEM image of $Mg_{0.7}Zn_{0.3}Fe_2O_4$ ferrite

To approximate the grain size, a histogram has been displayed in inset Fig. 6. From this histogram (inset of Fig. 6), the grain size has been evaluated to be 91.68 nm. Some of the experimental reports reveal that the magnesium ferrite bears the porous microstructure, which also supports our experimental study [21, 22, 24]. In Fig. 6, the nanopores are visible near the surface grain boundaries. H_2O dissociate into hydronium and hydroxide ions as a consequence of the chemidissociation on the ferrite pellet surface [2]. The hydroxide ions form chemical interactions with the unsaturated surface cations and break apart the physically bound water molecules that are adsorbed, which are held together by hydrogen bonds. The nanopores that allow certain H_3O^+ ions to be trapped, create enough electrostatic potential [1-2]. The potential further separates the physically adsorbed H_2O into their corresponding ions, and when the ions move in the direction of the electrodes, electricity is produced. Good porosity, evaluated theoretically in XRD studies, indicates that material may be considered for the generation of hydroelectric cell current [12-16].

3.3 HRTEM analysis

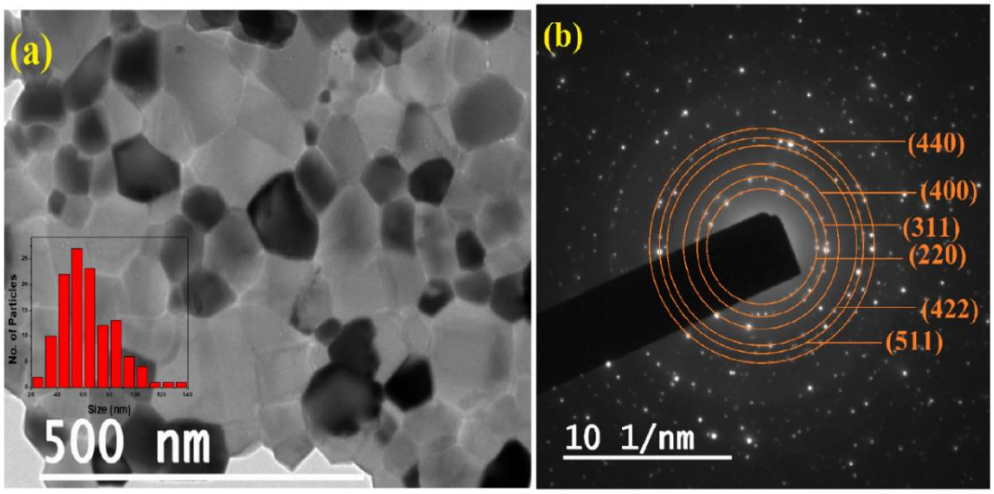

Fig. 7 HRTEM image (a) Microstructure (b) SAED pattern of $Mg_{0.7}Zn_{0.3}Fe_2O_4$ ferrite

The microstructure and SAED pattern are shown in Fig. 7(a-b), respectively, which collectively show HR-TEM imaging of the prepared Zn-Mg ferrite.

The inset image of the histogram in Fig. 7 (a) has been used to calculate the sample's average particle size, which was observed to be 63.76 nm. Observations from Fig. 7 (b) show that the hkl diffraction planes are (220), (311), (400), (422) (511) and (440). The strongest of these planes is (311) in comparison to the others. The diffraction dots in the SAED image suggest that the sample is thoroughly crystallized, and sample's numerous different planes represent its polycrystallinity. The particle size became larger in comparison to the sample's crystallite size. This might be a result of the nanoparticles' agglomerating together due to magnetic attraction [18].

3.4 FTIR Spectroscopy

Fig. 8 displays the FTIR bands of $MgFe_2O_4$ nanocrystalline material at 800 ºC for 2 h. The possible composition of the synthesized magnesium ferrite material is tentatively identified using FTIR spectroscopy. The wavenumber locations have been found at 418 cm^{-1}, 547 cm^{-1}, 1381 cm^{-1}, 1638 cm^{-1} and 3438 cm^{-1}. The vibrations of 418 cm^{-1} and 547 cm^{-1} represent the Fe-O and Mg-O bond stretching, respectively. The higher wavenumbers at 1638 cm^{-1} and 3446 cm^{-1} represent the vibration bands due to H_2O molecules. Similar wavenumbers have also been reported in previous research works, and thus the phase formation of cubic ferrite can be strongly defended [21-25]. Surface of Zn-substituted ferrite exhibit a prominent absorption of water molecules near 1638 cm^{-1} and 3438 cm^{-1}. The greater chemidissociation of water into H_3O^+ and OH^- caused by the greater water absorption on the surface may improve current output in $Mg_{0.7}Zn_{0.3}Fe_2O_4$ fabricated hydroelectric cells [18]. The current generation has been explained in V-I polarization study of the fabricated hydroelectric cell. The vibration modes are given in Table 2.

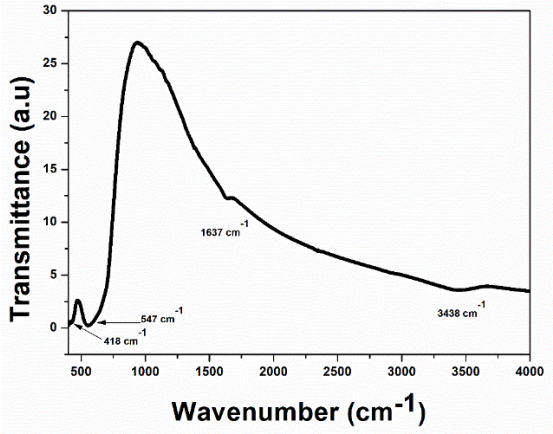

Fig. 8 FTIR analysis of zinc substituted magnesium ferrite.

Table 2. FTIR vibration bands of $MgFe_2O_4$ at 800 ℃ for 2 h

Wavenumber (cm^{-1})	Vibration mode
418	Fe-O stretching
547	Mg-O stretching
1381	NO_3^{2-} symmetric vibration
1637	H_2O bending vibration
3438	OH^- stretching vibration

3.5 PL Spectroscopy:

In order to examine defects and O_2 vacancies in the prepared ferrite, the room temperature PL spectroscopy was performed with the excitation wavelength of 350 nm, which is demonstrated in Fig. 9. The emission wavelength was noticed between 457 nm and 523 nm in the visible range. The emission spectra consist of a strong blue emission (457-488 nm), and comparatively weak green emission (530-523 nm). At 480 nm, the maximum peak emission was located. The best explanations for PL emission involve two distinct phenomena or mechanisms. The radiative imperfections in spinel ferrite that are located near surface grain boundaries, are caused by a strong blue emission [26–29]. The greenish PL emissions are caused by O_2 vacancies in the produced ferrite [28, 29]. The emission peaks from PL spectroscopy were observed to be consistent with several of the earlier investigations on ferrite nanoparticles [19, 26, 29]. Such PL emissions are indicated by the emergence of new energy bands close to the crystalline material's conduction and valence bands as a result of the increase in

intrinsic defects. Significant oxygen vacancies and radiative defects are observed in the PL spectral region between 456 and 520 nm. W-H analysis has confirmed that the crystal imperfections in this sample are due to micro strain. These electron-absorbing oxygen defects have a strong affinity to OH^- in water. When H_2O gets close to the oxygen void defect pairs, it splits into H_3O^+ and hydroxide ions. Thus, the surface rich oxygen vacancies and the radiative defects make the material a potential candidate for HEC application.

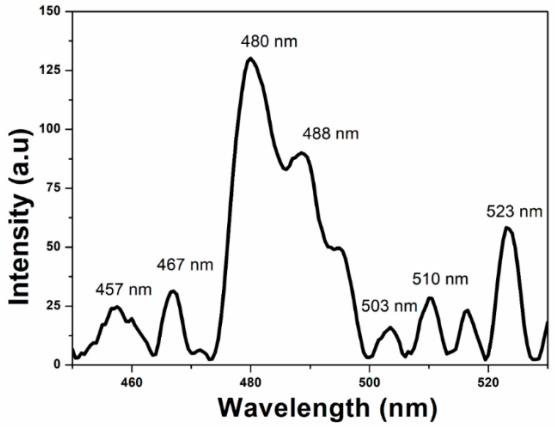

Fig.9 PL spectroscopy of $Mg_{0.7}Zn_{0.3}Fe_2O_4$.

3.6 HEC Performance

The V-I polarization plot of $Mg_{0.7}Zn_{0.3}Fe_2O_4$ based wet hydroelectric cell (HEC) was obtained to investigate green electricity generation. Figure 10 represents the voltage, current and power (P) plot of prepared wet HEC. The open circuit voltage (V_{oc}) of the prepared hydroelectric cell was measured 0.823 V and short circuit current (I_{sc}) was 7 mA. The measured offload power was 5.76 mW. The V-I plot, illustrated in Fig. 10, has 3 dissimilar regions: concentration loss domain (C-D), ohmic loss region (B-C), and activation loss zone (A - B). Ion transfers only occurs when the energy barrier is surpassed, and the minimum standard of energy required to do so is known as activation energy. The activation loss, that typically arises near low currents, is the loss experienced when overcoming the energy barrier [30–38].

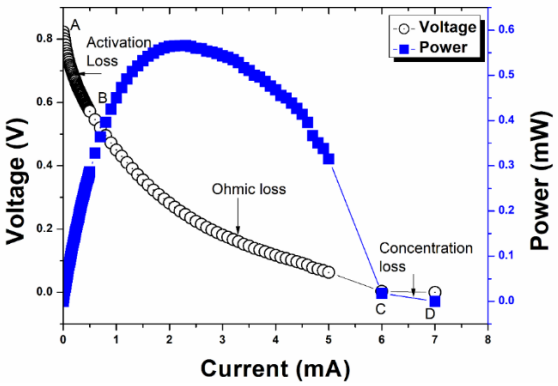

Fig. 10 V-I polarization plot of Wet $Mg_{0.7}Zn_{0.3}Fe_2O_4$ based HEC

Due to ion mobility through the ferrites' nanopores, a considerable resistance is produced after surpassing the energy barrier. This area is referred to as the ohmic zone and therefore is linear. Very reactive insufficient ions that are accessible for the electrodes cause the concentration loss. The electronegativity of surface cations, porosity, and the oxygen voids all have a significant impact on the current output in HEC [30, 31]. The pull of electron lone pairs in H_2O caused by the relatively electronegative Fe^{3+} drives the breakdown of water molecules into ionized species and is the source of current production in the ferrite-fabricated HEC [32–35]. Hydroelectric cells may generate current as a result of two significant occurrences, ie. the chemidissociation of H_2O and its physiorption of via H-bonding [36–38]. The process of water molecules dissociating into H_3O^+ and OH^- ions, known as chemisissociation, is made easier by the significant attraction of lone pairs of H_2O. The dissociated ions link with unsaturated surface cations and surface oxygen anions after chemidissociating H_2O, forming a surface chemisorbed layer. Moreover, by hydrogen bonding, the chemisorption of OH^- promotes physisorption of H_2O [34–38]. Oxygen vacancies, also known as voids, have previously been said to aid in the chemidissociation of H_2O and to serve as the key sites for this reaction [30–38]. Following the dissociation, the ions become trapped in the ferrites' nanopores and

produce the required electric potential [30–38]. The physically adsorbed H_2O is further dissociated by this potential. The hydroelectric cell produces the electricity through this iterative process via Grotthus chain mechanism. The electrochemical redox reactions at electrodes may be given as:

At anode (Zn),

$$Zn + 2OH^- \longrightarrow Zn(OH)_2 + 2e$$

At cathode (Ag),

$$2H_3O^+ + 2e \longrightarrow H_2O + H_2$$

The presence of porous structure, grain boundary defect and the oxygen deficiencies in the processed ferrite can be evidenced from the XRD, FESEM and photoluminescence studies. Thus, the prepared ferrite has been used for developing the hydroelectric cell. The present study reveals comparatively higher current than some of the earlier reported works of HEC fabricated using TiO_2, ZnO, Al_2O_3, MgO, silicon dioxide, $CoFe_2O_4$ etc. [13, 38].

3.7 Impedance Analysis

Impedance analysis of the fabricated wet HEC was performed at ambient temperatures in order to examine the electrical characteristics of the prepared wet hydroelectric cell. Figure 11 shows the impedance plot (also known as the Nyquist plot) of the wet HEC pellet. The original Nyquist plot derived from the experimental results is represented by the black curve, while the fitted Nyquist plot is shown by the red curve in Fig. 11. The semi-circular graph in the upper and intermediate frequency ranges, respectively, represents the impedance resulting from bulk and charge transfer at the grain boundary contact [30-35]. Similar to this, the migration of the ions is represented by a tail in the low-frequency band [30-35]. With the existing impedance measurements, an analogous electrical circuit has been created employing Nyquist plot fitting to analyze the resistance and capacitances caused by grains, grain boundary interface, and materials. In the analogous circuit (shown in Fig. 11), CPE_1 stands for the charge transfer capacitance, C_1 for the bulk capacitance, Ws for the Warburg impedance, R_1 is the series resistance, R_2 for charge transfer resistance, and R_3 for bulk resistance. CPE_1 stands for constant phase component, and it exhibits non-ideal capacitive behaviour [30]. The increased rate of reactions at the electrodes is caused by the charge transfer resistance R_2 [33]. Warburg impedance presence suggests that ions have diffused more effectively towards Zn/Ag electrodes [33]. As a result of improved cation-oxygen vacancies, there are more ions available at the electrodes, which causes water to dissociate to a higher extent. A slow flow of ions towards the electrodes is indicated by the high bulk resistance value (R_3) [33]. Although the ions migrate slowly, the HEC fabricated with this material has a 7 mA output current due to low charge transfer resistance (R_2) and the warburg impedance (Ws). The following Table 3 represents the obtained values of all the electrical components.

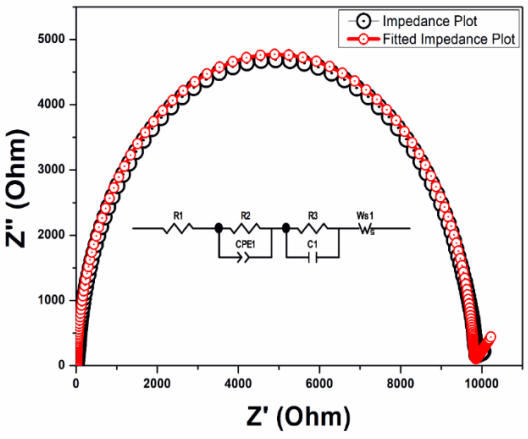

Fig. 11 Nyquist plot of $Mg_{0.7}Zn_{0.3}Fe_2O_4$ based wet HEC

Table 3: Fitted electrical parameters of impedance plot

Materials	R1 (Ω)	R2(Ω)	R3(Ω)	CPE1	C1	Ws
$Mg_{0.7}Zn_{0.3}Fe_2O_4$	21.97	133.8	9863	9.78×10^{-11}	9.74×10^{9}	264.9

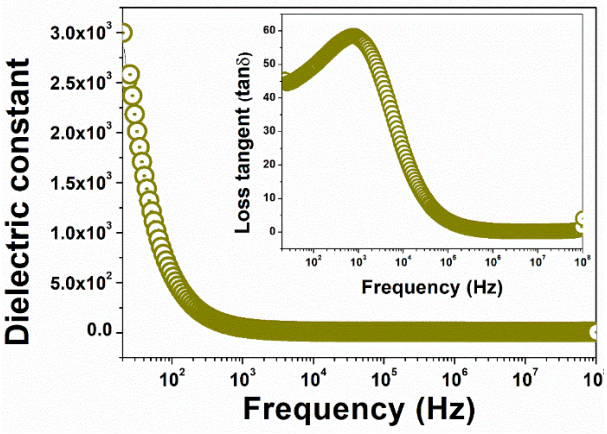

Fig 10 Dielectric constant and loss tangent plot of $Mg_{0.7}Zn_{0.3}Fe_2O_4$ based wet HEC

The equations given below have been used to compute the ferrite samples' dielectric constant (k) [39]:

$$C = \frac{\epsilon_0 \epsilon_r A}{d}, \quad (9)$$

$$k = \epsilon_r , \quad (10)$$

Here, C denotes capacitance, ϵ_0 refers to permittivity of free space, ϵ_r defines the relative permittivity and others have their usual meanings [39-46]. In Fig. 10, the dielectric constant (k) variability of the produced ferrite materials with reference to frequency is depicted (a). k rises at low frequencies due to the predominance of the dipolar and interfacial polarizations. Moreover, at higher frequencies, the dipolar polarization falls off and the electronic polarization rises, which reduces k and causes frequency independent instability [39, 40]. Many research studies have provided an explanation for how the dielectric constant decreases as frequency rises [38–46]. Spinel ferrites frequently exhibit a decrease in dielectric constant with increasing frequency, which supports Koop's theory [47]. Figure 10 (b) represents the loss tangent Vs frequency plot of the prepared ferrite. The dielectric loss plots indicate peak near 700 Hz, with a high dielectric loss. The grain boundary relaxation of the charge carriers is responsible for such type of peak in the prepared ferrite. At low frequencies, the dielectric loss is high, whereas at high frequencies it reduces. Increased grain boundary resistance that is linked to dopants and defects at grain boundary, can occur more easily as a result of grain boundary relaxation [18]. The high dielectric constant of zinc substituted ferrite-based HEC pellet may be due to the increased value of capacitance. The higher capacitance or dielectric constant of Zn-substituted HEC pellets is also because of the interfacial or surface charges produced by the splitted ions (H_3O^+ and hydroxyl ions) near electrodes as well as within lattice [18]. The dipole-dipole relaxation of H_3O^+/OH^- hopping about the defective sites may be the cause of a significant loss peak between 100 Hz and 10 kHz [18].

Conclusion:

The nanocrystalline $Mg_{0.7}Zn_{0.3}Fe_2O_4$ material has been synthesized by sol-gel technique, whose cubic phase having crystallite size of 30.79 nm was identified by XRD. The wavenumbers 418 cm^{-1} and 547 cm^{-1}, studied by FTIR spectroscopy, also indicate the spinel phase formation. The lattice strain evaluated by W-H plot is responsible for the crystal disorders in the prepared ferrite. The crystal disorders are responsible for defective surface grain boundaries, porosity and the oxygen vacancies in the prepared ferrite, which greatly impact on the hydroelectric cell behaviour of prepared ferrite. The theoretical porosity, 40.2 %, has been evaluated by XRD, which is also observed from the FESEM micrographs of the produced ferrite bearing the average grain

size of 91 nm. HRTEM studies indicate increased particle size near 64 nm due to the magnetic attraction between the nanoparticles, and the bright diffraction rings indicate polycrystallinity of nanoferrite. Besides these, the PL studies reveal various defects such as grain boundary defect and O_2 vacancies in synthesized ferrite corresponding to the emission wavelength ranging from 457 nm to 523 nm. These defects on the surface of ferrite pellet are responsible for water chemidissociation into H_3O^+ and OH^- ions. The trapping of H_3O^+ ions in nanopores create adequate electric potential to split more water molecules. The impedance studies reveal sufficient charge transfer resistance and Warburg impedance, which are responsible for the fast reactions at electrodes and better diffusion of ions towards the electrode. This phenomenon supports the generation of electric currents in the ferrite prepared hydroelectric cell. Furthermore, the high purity H_2 gas, liberated at Ag-electrode, may be used in H_2 powered vehicles in near future. The prepared ferrite fabricated HEC displayed 7 mA offload current with the offload power of 5.63 mW. Thus, a non-conducting surface of ferrite facilitates the spontaneous dissociation of H_2O at room temperature to generate green electricity.

Acknowledgements

Aryabhatta Center for Nanoscience and Nanotechnology, Aryabhatta Knowledge University Patna and Deptt. of Higher Education, Govt. of Bihar, provided the necessary infrastructures for the authors to conclude this research.

Conflict of interest

The authors do not have any conflict of interest

References:

[1] J. Shah, R. Kumar Kotnala, Rapid green synthesis of ZnO nanoparticles using a hydroelectric cell without an electrolyte, J. Phys. Chem. Solid. 108 (2017) 15-20,

[2] Das, R, Shah, J, Sharma, S, Sharma, PB, Kotnala, RK. Electricity generation by splitting of water from hydroelectric cell: An alternative to solar cell and fuel cell. Int J Energy Res. 2020; 44: 11111– 11134. https://doi.org/10.1002/er.5698

[3] R.K. Kotnala, J. Shah, Lithium-substituted Magnesium Ferrite Material Based Hydroelectric Cell and Process for Preparation Thereof, US 2016/0285121 A1, 2016.

[4] R.K. Kotnala, J. Shah, 2.8 magnetic materials, in: Compr. Energy Syst., Elsevier, 2018, pp. 204-234, https://doi.org/10.1016/B978-0-12-809597-3.00219-4.

[5] W. Montha, W. Maneeprakorn, N. Buatong, I.M. Tang, W.P. On, Synthesis of doxorubicin-PLGA loaded chitosan stabilized (Mn, Zn) Fe_2O_4 nanoparticles: biological activity and pH-responsive drug release, Mater. Sci. Eng. C 59 (2016) 235–240.

[6] J. Wu, W. Jiang, Y. Shen, W. Jiang, R. Tian, Synthesis and characterization of mesoporous magnetic nanocomposites wrapped with chitosan gatekeepers for pH sensitive controlled release of doxorubicin, Mater. Sci. Eng. C 70 (2017) 132–140.

[7] A. Bigham, F. Foroughi, M. Motamedi, M. Rafienia, Multifunctional nanoporous magnetic zinc silicate-$ZnFe_2O_4$ core-shell composite for bone tissue engineering applications, Ceram. Int. 44 (2018) 11798–11806.

[8] G. Wang, F. Zhou, X. Li, J. Li, Y. Ma, J. Mu, Z. Zhang, H. Che, X. Zhang, Controlled synthesis of L-cysteine coated cobalt ferrite nanoparticles for

drug delivery, Ceram. Int. 44 (2018) 13588–13594.

[9] E.M.M. Ramosn, V.G. Chavez, B.I. Macias-Martínez, C.M. Lopez-Badillo, L.A. García-Cerda, Synthesis and characterization of maghemite nanoparticles for hyperthermia applications, Ceram. Int. 41 (2015) 397–402

[10] P. Heidari, S.M. Masoudpanah, Structural, magnetic and optical properties and photocatalytic activity of magnesium-calcium ferrite powders, Journal of Physics and Chemistry of Solids, Volume 148,2021,109681

[11] Kotnala, R. K., Jyoti Shah, Bhikham Singh, Sukhvir Singh, S. K. Dhawan, A. Sengupta. Humidity response of Li-substituted magnesium ferrite. Sensors and Actuators B: Chemical 129, (2008) 909-914

[12] R.K. Kotnala, J. Shah, Green hydroelectrical energy source based on water dissociation by nanoporous ferrite, Int. J. Energy Res. 40 (2016) 1652-1661, https://doi.org/10.1002/er.3545.

[13] J. Shah, K.C. Verma, A. Agarwal, R.K. Kotnala, Novel application of multiferroic compound for green electricity generation fabricated as hydroelectric cell, Materials Chemistry and Physics. 239 (2020).

https://doi.org/10.1016/j.matchemphys.2019.122068.

[14] S. Saini, J. Shah, R.K. Kotnala, K.L. Yadav, Nickel substituted oxygen deficient nanoporous lithium ferrite based green energy device hydroelectric cell, J Alloy Compd. 827(2020) 154334.

https://doi.org/10.1016/j.jallcom.2020.154334

[15] Kotnala, RK, Saini, S, Shah, J, Yadav, KL. Significant role of defect-induced surface energy in water splitting to generate electricity by nickel ferrite hydroelectric cell. Int J Energy Res. 2022; 46 (5): 6421- 6435.

https://doi.org/10.1002/er.7579

[16] Sandeep Saini, K. L. Yadav, Jyoti Shah, and R. K. Kotnala, Enhanced Water Splitting by Strained Lithium-Substituted Nickel Ferrite Hydroelectric Cells, ACS Applied Energy Materials (2022)

https://doi.org/10.1021/acsaem.2c00708

[17] Manash, A., Singh, R.K., Kumar, V. et al. Studies on structural and optical behavior of nanoporous potassium-substituted magnesium ferrite nanomaterials, and their application as a hydroelectric cell. J Mater Sci: Mater Electron 33, 22103–22118 (2022).

https://doi.org/10.1007/s10854-022-08978-0

[18] Kumar, V., Singh, R.K., Manash, A. et al. Structural, optical and electrical behaviour of sodium-substituted magnesium nanoferrite for hydroelectric cell applications. Appl Nanosci (2022). https://doi.org/10.1007/s13204-022-02737-7

[19] Das S.B, Singh R.K, Kumar V, Kumar N, Singh P, Naik N.K, Structural, magnetic, optical and ferroelectric properties of Y^{3+} substituted cobalt ferrite nanomaterials prepared by a cost-effective sol-gel route. Mater Sci Semicond Process. 145, 106632 (2022)

https://doi.org/10.1016/j.mssp.2022.106632

[20] Shankar, U., Singh, R.K., Das, S.B. et al. Studies on the Structural Properties and Band Gap Engineering of Ag^{+}-Modified $MgFe_2O_4$ Nanomaterials Prepared by Low-Cost Sol–Gel Method for Multifunctional Application. J Supercond Nov Magn 35, 1937–1960 (2022). https://doi.org/10.1007/s10948-022-06220-w

[21] Jacob George, Abraham K.E., Gas sensing characteristics of magnesium ferrite and its doped variants, Physica B: Condensed Matter, 610,2021,412958, https://doi.org/10.1016/j.physb.2021.412958

[22] Rohit R. Powar, Varsha D. Phadtare, Vinayak G. Parale, Sachin Pathak, Kallapa R. Sanadi, Hyung-Ho Park, Devidas R. Patil, Pravina B. Piste, Dnyandevo N. Zambare, Effect of zinc substitution on magnesium ferrite nanoparticles: Structural, electrical, magnetic, and gas-sensing properties, Materials Science and Engineering: B,262,2020,114776, https://doi.org/10.1016/j.mseb.2020.114776

[23] A Nigam, S.J. Pawar, Structural, magnetic, and antimicrobial properties of zinc doped magnesium ferrite for drug delivery applications, Ceram.Int.l, 46 (2020) 4058-4064

[24] C. Choodamani, B. Rudraswamy, G.T. Chandrappa, Structural, electrical, and magnetic properties of Zn substituted magnesium ferrite, Ceram Int, 42, 2016, 10565-10571

https://doi.org/10.1016/j.ceramint.2016.03.120

[25] Kumar, Vivek, Nishant Kumar, Shashank Bhushan Das, Rakesh Kumar Singh, Kakali Sarkar, Manish Kumar. Sol-gel assisted synthesis and tuning of structural, photoluminescence, magnetic and multiferroic properties by annealing temperature in nanostructured zinc ferrite. Materials Today: Proceedings 47 (2021): 6242-6248.

[26] S B Das, V Kumar, Md. Muzzammilul Haque Siddiqui, Nishant Kumar, Rakesh Kumar Singh, Rajneesh Kumar, Structural characterization and investigation of magneto-optic and multiferroic properties of nanostructured CoFe2O4 prepared by sol–gel derived facile chemical route, Materials Today: Proceedings, 49, 2022, 1481-1489, https://doi.org/10.1016/j.matpr.2021.07.234

[27] C H Zang, D M Zhang, C J Tang, S J Fang, Z J Zong, Y X Yang, C H Zhao, Y S Zhang, J. Phys. Chem. C113 (2009) 18527

[28] L J Zhuge, X M Wu, Z F Wu, X M Yang, X M Chen, Q Chen, J. Mater. Chem. Phys.120 (2010) 480

[29] T M. Hammad, J K. Salem, A A. Amsha, N K. Hejazy, J of Alloys and Compounds 741 (2018) 123-130

[30] Jyoti Shah, Abha Shukla, R. K. Kotnala, Highly Accelerated, Sustainable, Abundant Water Splitting at Room Temperature Generating Green Electricity by Sb-Doped SnO_2 Hydroelectric Cell, ACS Sustainable Chem. Eng.2021, 9, 15229−15238 https://doi.org/10.1021/acssuschemeng.1c04899

[31] R. Gupta, J. Shah, R. Singh, R.K. Kotnala, Nonphotocatalytic Water Splitting Process to Generate Green Electricity in Alkali Doped Zinc Oxide Based Hydroelectric Cell, Energy and Fuels. 35 (2021) 9714–9726.

https://doi.org/10.1021/acs.energyfuels.1c01164.

[32] J. Shah, S. Jain, A. Shukla, R. Gupta, R.K. Kotnala, A facile non-photocatalytic technique for hydrogen gas production by hydroelectric cell, Int. J. Hydrogen Energy 42 (2017) 30584-30590, https://doi.org/10.1016/j.ijhydene.2017.10.105.

[33] R.K. Kotnala, Rojaleena Das, Jyoti Shah, Sanjeev Sharma, C. Sharma, P.B. Sharma, Red mud industrial waste translated into green electricity production by innovating an ingenious process based on Hydroelectric Cell,

Journal of Environmental Chemical Engineering,10 (2), 2022,107299

https://doi.org/10.1016/j.jece.2022.107299

[34] Saini S, K L. Yadav, J Shah, R K. Kotnala. "Effect of Li^{+}, Mg^{2+}, and Al^{3+} Substitution on the Performance of Nickel Ferrite-Based Hydroelectric Cells." Energy & Fuels (2022)

https://doi.org/10.1021/acs.energyfuels.2c01244

[35] Shah J, Shukla A, Gupta G, Kar M, Jain S, Kotnala RK. ZnO Nanoflakes Self-assembled from Water Splitting Process by Hydroelectric Cell. Reaction Chemistry & Engineering. 2022 https://doi.org/10.1039/D2RE00094F

[36] P. Kumar, S. Vashishth, I. Sharma, V. Verma, Porous SnO_2 ceramic-based hydroelectric cells for green power generation, Journal of Materials Science: Materials in Electronics. 32 (2021) 1052–1060. https://doi.org/10.1007/s10854-020-04880-9

[37] R. Gupta, J. Shah, R. Das, S. Saini, R.K. Kotnala, Defect-mediated ionic hopping and green electricity generation in $Al_{2-x}Mg_xO_3$-based hydroelectric cell, Journal of Materials Science. 56 (2021) 1600–1611. https://doi.org/10.1007/s10853-020-05280-4

[38] R.K. Kotnala, R. Gupta, A. Shukla, S. Jain, A. Gaur, J. Shah, Metal Oxide Based Hydroelectric Cell for Electricity Generation by Water Molecule Dissociation without Electrolyte/Acid, Journal of Physical Chemistry C. 122 (2018) 18841–18849

[39] K. Sarkar,V. Kumar, S. Mukherjee, Synthesis and investigation of properties of nanostructured cubic PMN ceramics for possible applications in electronics, J Mater Sci: Mater Electron 31 (2020), 14314-14321

[40] J.C.R. Araujo, S. Araujo-Barbosa, A.L.R. Souza et al., Tuning structural, magnetic, electrical, and dielectric properties of $MgFe_2O_4$ synthesized by sol-gel followed by heat treatment, Journal of Physics and Chemistry of Solids, 154, 2021, 110051, https://doi.org/10.1016/j.jpcs.2021.110051

[41] J.A. Boukhari, A. Khalaf, R. Awad, Structural analysis and dielectric investigations of pure and rare earth elements (Y and Gd) doped nio nanoparticles, J. Alloys Compd. 820 (2020) 153381,

https://doi.org/10.1016/j.jallcom.2019.153381

[42] K. Sarkar, S. Mukherjee, S. Mukherjee, Structural, electrical and magnetic behaviour of undoped and nickel doped nanocrystalline bismuth ferrite by solution combustion route, Processing and Application of Ceramics 9 (2015) 53-60

[43] Sarkar K, Kumar V, Das S B, Kumar M, Srivastava R (2022) Investigation of opto-electronic properties and morphological characterization of magnesium niobate ceramics synthesized by two-stage process, Mater. Today: Proc. 49 446-452

[44] Sarkar K, Mukherjee S (2016) Synthesis, Characterization and Property Evaluation of Single Phase $MgNb_2O_6$ by Chemical route; J. Aust. Ceram. Soc. 52: 32-40

[45] Sarkar K, Kumar V, Mukherjee S (2017), Synthesis, Characterization and Property Evaluation of Single Phase $Mg_4Nb_2O_9$ by two stage process; J. T. Indian Ceram. Soc. 76: 43-49

[46] Sarkar, Kakali, Abhishek Kumar, Sharad Chandra Pandey, Saurabh Kumar, Vivek Kumar. Tailoring the structural, optical, and dielectric

properties of nanocrystalline niobate ceramics for possible electronic application. International Research Journal on Advanced Science Hub 05. (2023) 01–07, 10.47392/irjash.2023.001

[47] C.G. Koops, On the dispersion of resistivity and dielectric constant of some semiconductors at audio frequencies, Phys. Rev. 83 (1951) 121–124, https://doi.org/10.1103/PhysRev.83.121